Supporting Information

Lysozyme-Assisted Photothermal Eradication of Methicillin-Resistant Staphylococcus aureus Infection and Accelerated Tissue Repair with Natural Melanosome Nanostructures

Jun Li,[†] Xiangmei Liu,*[,‡] Ziao Zhou,[‡] Lei Tan,[‡] Xianbao Wang,[‡] Yufeng Zheng,[§] Yong Han,[∥] Da-Fu Chen,[⊥] Kelvin Wai Kwok Yeung,[#] Zhenduo Cui,[†] Xianjin Yang,[†] Yanqin Liang,[†] Zhaoyang Li,[†] Shengli Zhu,[†] Shuilin Wu*[,†,‡]

[†] The Key Laboratory of Advanced Ceramics and Machining Technology by the Ministry of Education of China, School of Materials Science & Engineering, Tianjin University, Tianjin 300072, China

[‡] Hubei Key Laboratory of Polymer Materials, Ministry-of-Education Key Laboratory for the Green Preparation and Application of Functional Materials, School of Materials Science & Engineering, Hubei University, Wuhan 430062, China

[§] College of Engineering, State Key Laboratory for Turbulence and Complex System, Department of Materials Science and Engineering, Peking University, Beijing 100871, China

[∥] State Key Laboratory for Mechanical Behavior of Materials, School of Materials Science and Engineering, Xi'an Jiaotong University, Xi'an, Shaanxi, 710049, China

[⊥] Beijing JiShuiTan Hosp, Beijing Res Inst Orthopaed & Traumatol, Lab Bone Tissue Engn, Beijing 100035, Peoples R China.

[#] Department of Orthopaedics & Traumatology, Li Ka Shing Faculty of Medicine, The University of Hong Kong, Pokfulam, Hong Kong 999077, China

1. Supplementary figure

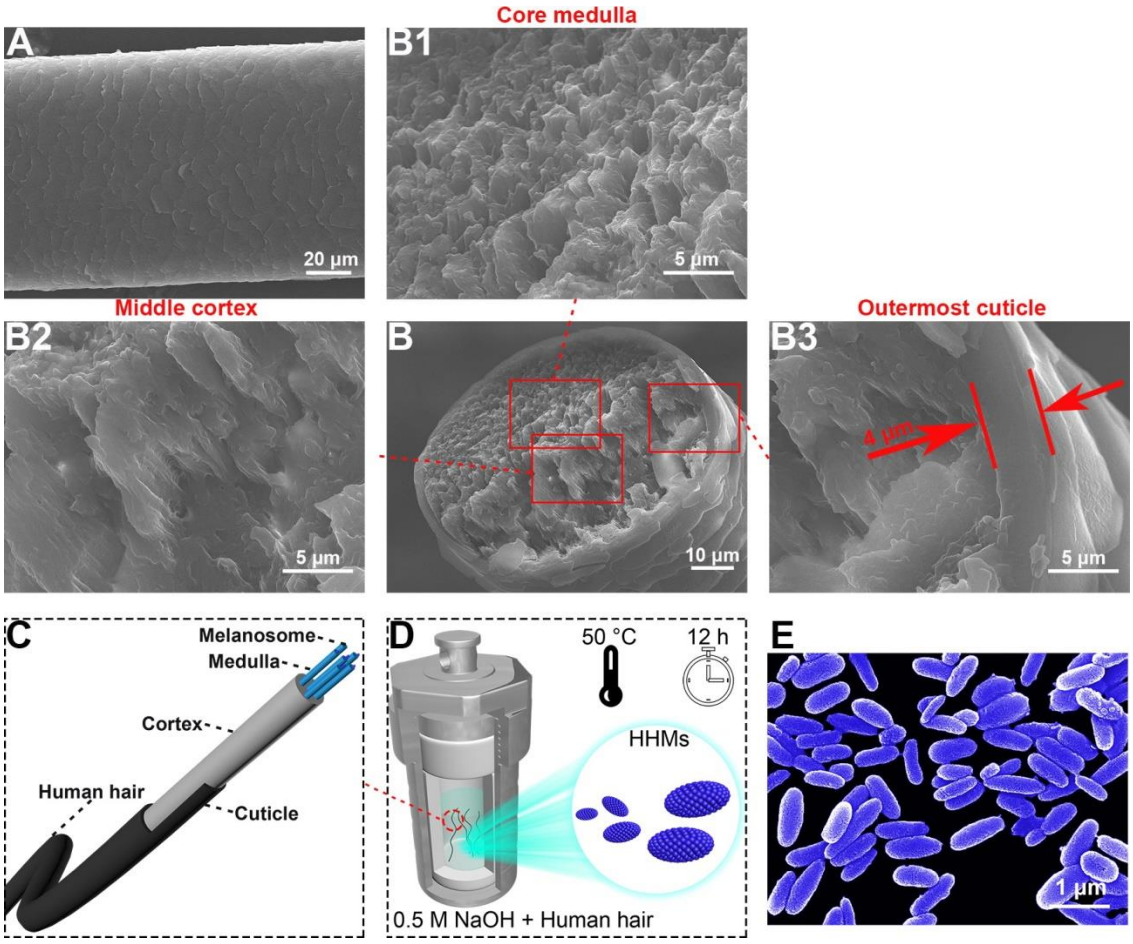

Figure S1. SEM images of a (A) planar and (B) sectional human hair fiber. SEM images of natural hierarchical structure of a sectional human hair fiber: (B1) core medulla, (B2) middle cortex, and (B3) outermost cuticle sheath. (C) Schematic illustration of natural hierarchical structure of human hair fiber. (D) Schematic illustration of preparation of HHMs by a "low-temperature alkali heat" method. (E) SEM images of relatively low magnification of HHMs.

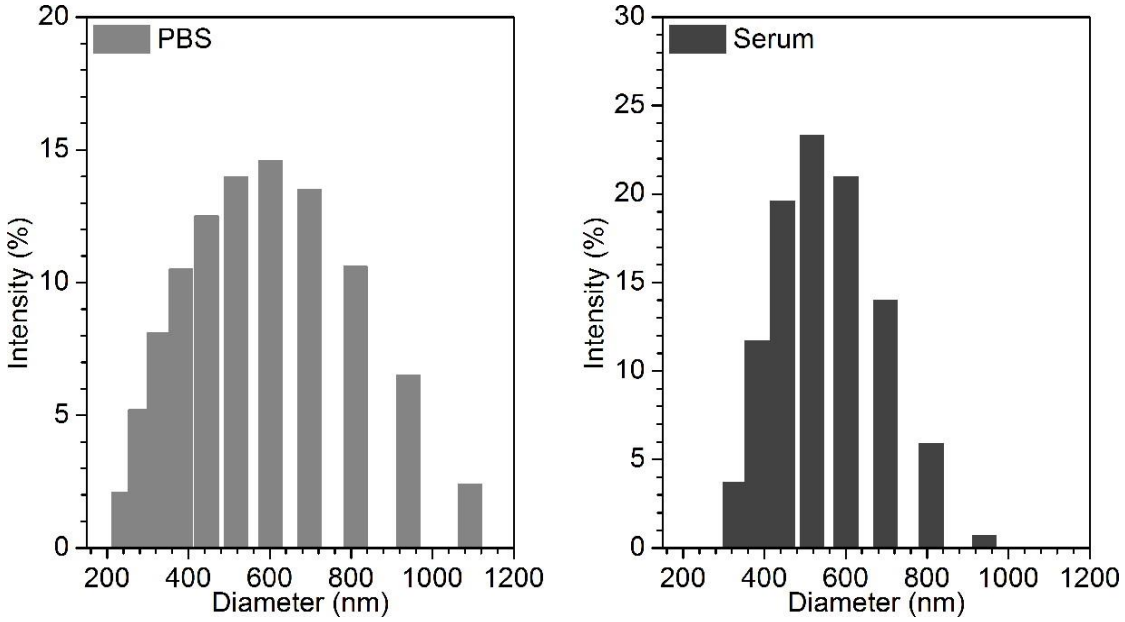

Figure S2. Hydrodynamic sizes of HHMs in PBS and serum by DLS.

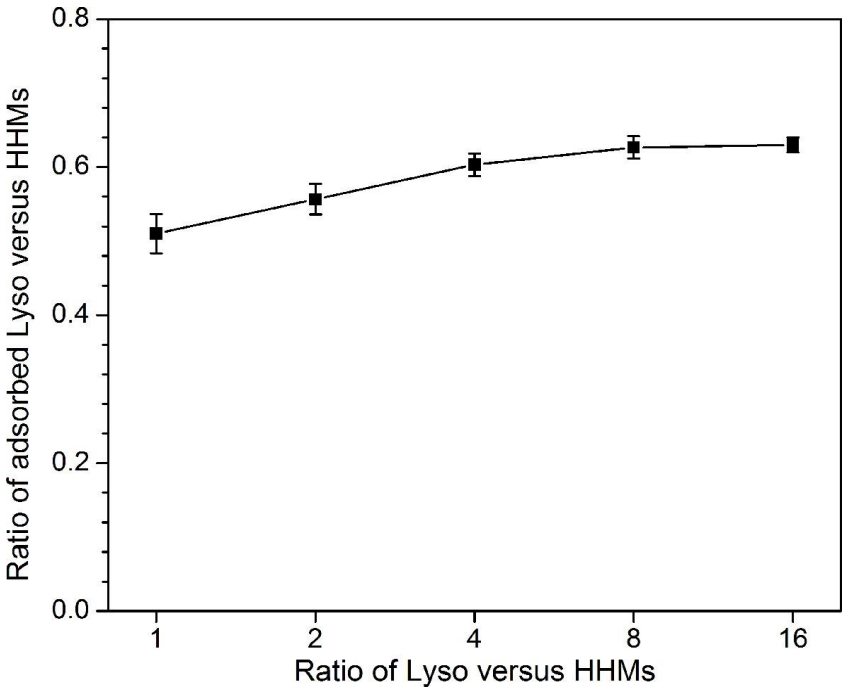

Figure S3. Mass ratios of adsorbed Lyso:HHMs by using different mass ratios of Lyso:HHMs. (n = 3). Error bars indicate means ± standard deviations.

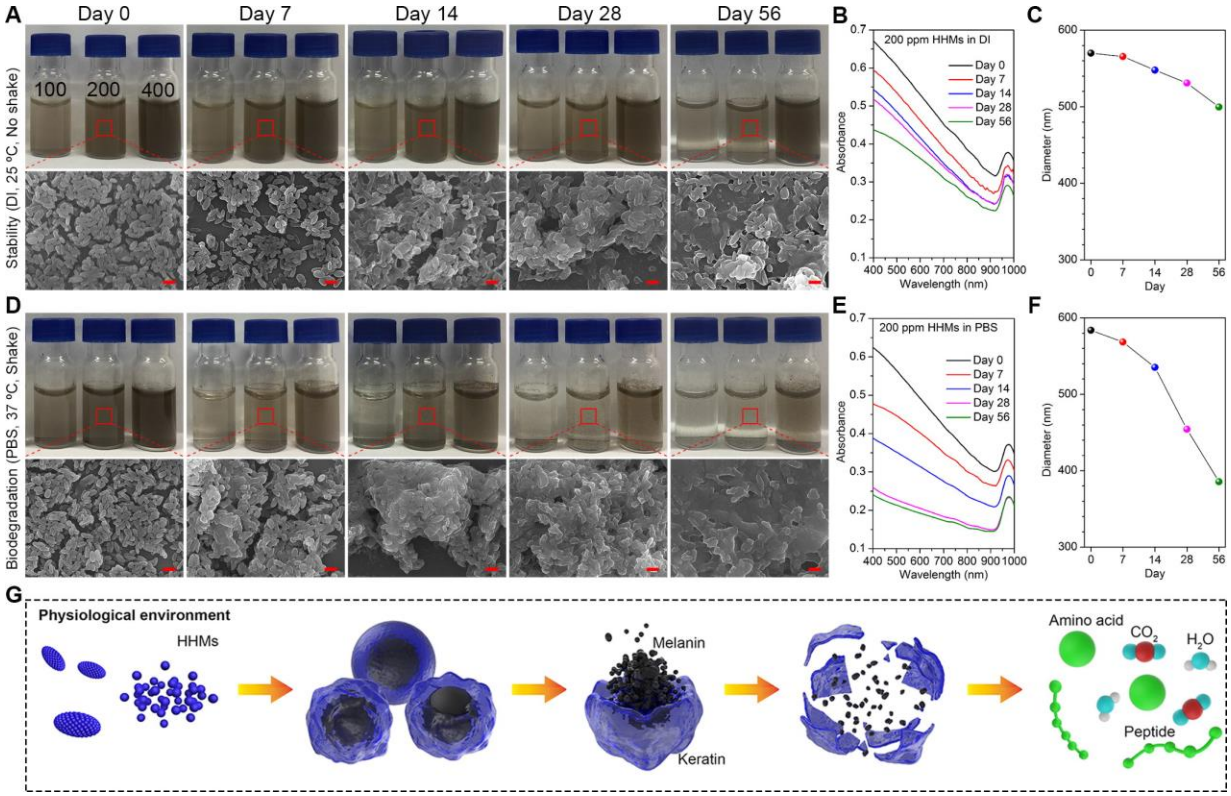

Figure S4. Biodegradation behavior of HHMs. (A) Digital photograph of HHMs (100, 200, and 400 ppm) and corresponding SEM images (scale bars = 1 μm) of 200 ppm HHMs in DI without shaking at 25 °C on days 0, 7, 14, 28, and 56. (B) Absorption spectra (400-1000 nm) of 200 ppm HHMs in DI without shaking at 25 °C on days 0, 7, 14, 28, and 56. (C) Hydrodynamic sizes of HHMs in DI without shaking at 25 °C on days 0, 7, 14, 28, and 56. (D) Digital photograph of HHMs (100, 200, and 400 ppm) and corresponding SEM images (scale bars = 1 μm) of 200 ppm HHMs in PBS (pH = 7.4) in a horizontal shaker at 37 °C on days 0, 7, 14, 28, and 56. (E) Vis-NIR absorbance spectra (400-1000 nm) of 200 ppm HHMs in PBS (pH = 7.4) in a horizontal shaker at 37 °C on days 0, 7, 14, 28, and 56. (F) Hydrodynamic sizes of HHMs in PBS (pH = 7.4) in a horizontal shaker at 37 °C on days 0, 7, 14, 28, and 56. (G) Schematic illustration of possible process of biodegradability of HHMs in physiological environment.

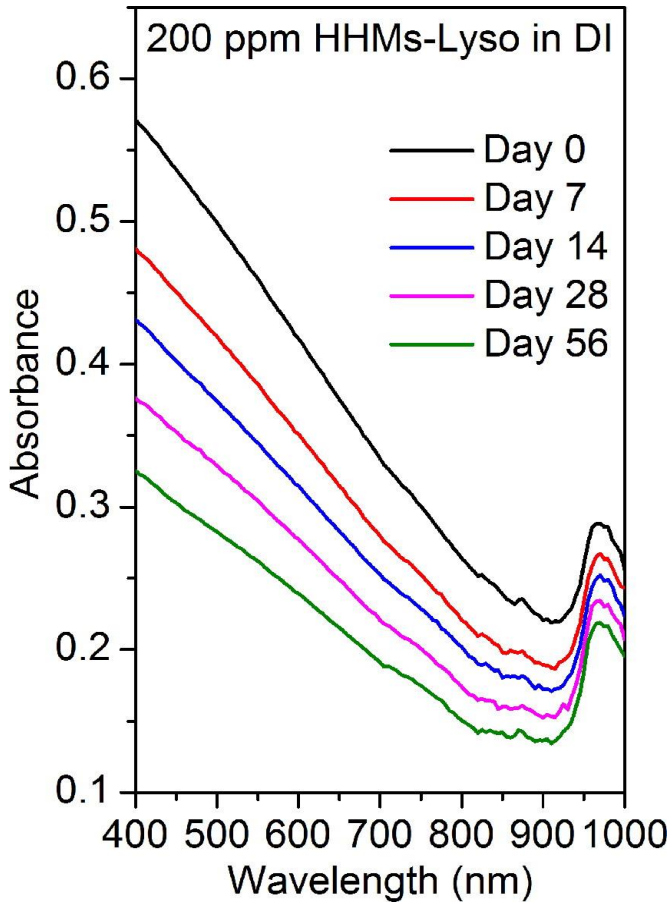

Figure S5. Absorption spectra (400-1000 nm) of 200 ppm HHMs-Lyso in DI without shaking at 25 °C on days 0, 7, 14, 28, and 56.

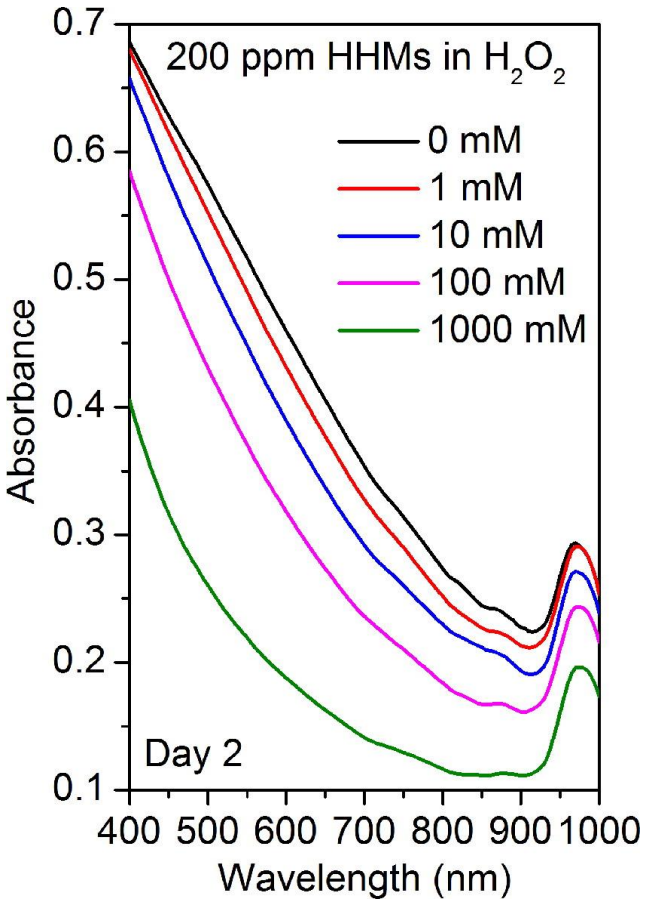

Figure S6. Absorption spectra of the HHMs (200 ppm) in H_2O_2 solutions with different concentrations (1, 10, 100, 1000 mM) on Day 2.

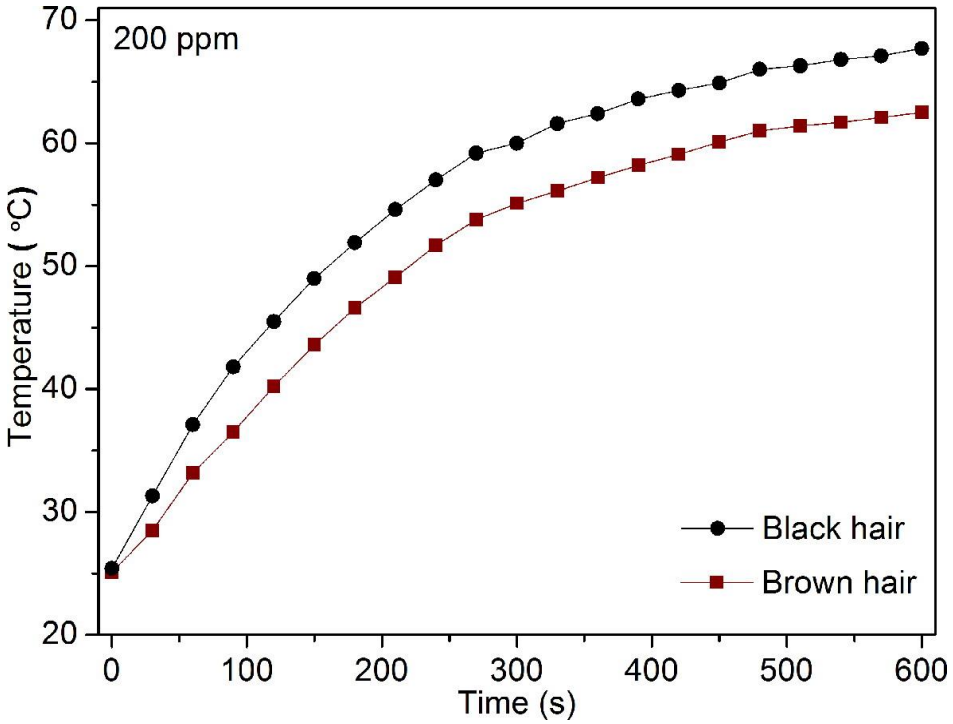

Figure S7. Photothermal heating curves of 200 ppm HHMs solutions extracted from black hair and brown hair in 10 min at 1.0 W cm^{-2}.

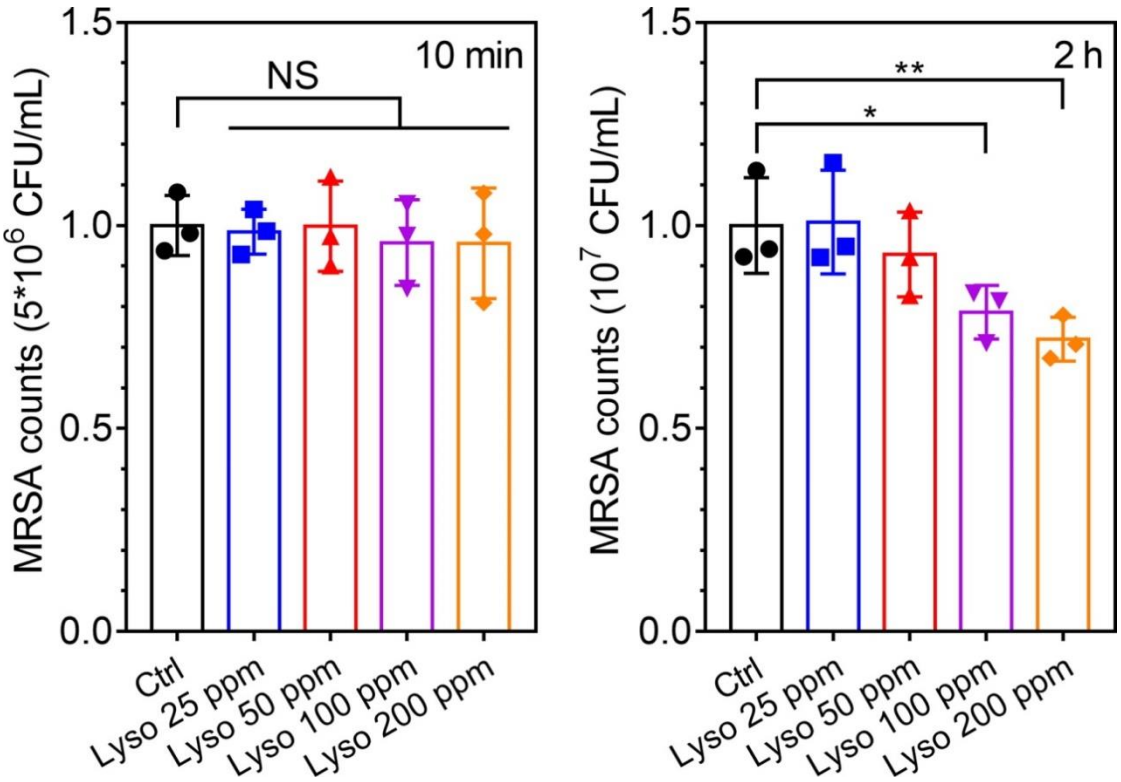

Figure S8. Antibacterial activity of free Lyso at varied concentrations (25, 50, 100, and 200 ppm) for (A) 10 min and (B) 2 h incubation (n = 3). (C) Antibacterial activity of adsorbed Lyso at varied concentrations (25, 50, 100, and 200 ppm) for 2 h incubation (n = 3). Error bars indicate means ± standard deviations: *P < 0.05, **P < 0.01 (t test). NS, not significant (P > 0.05).

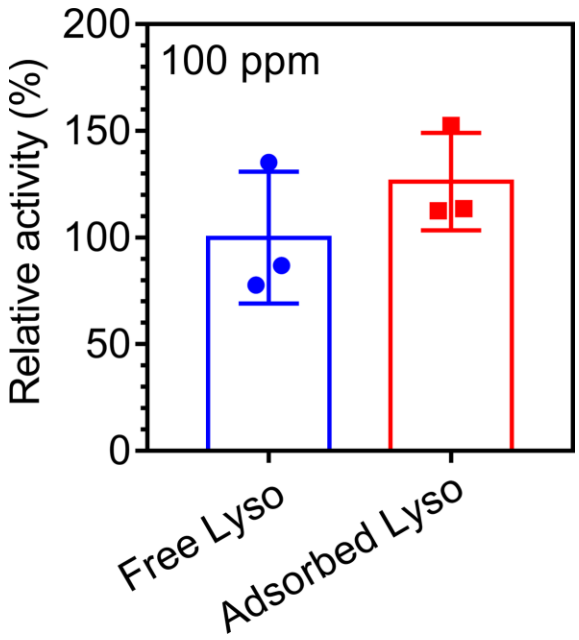

Figure S9. Relative activities of free Lyso and adsorbed Lyso (HHMs-Lyso) in the case of the same concentration of Lyso (100 ppm) (n = 3). Error bars indicate means ± standard deviations.

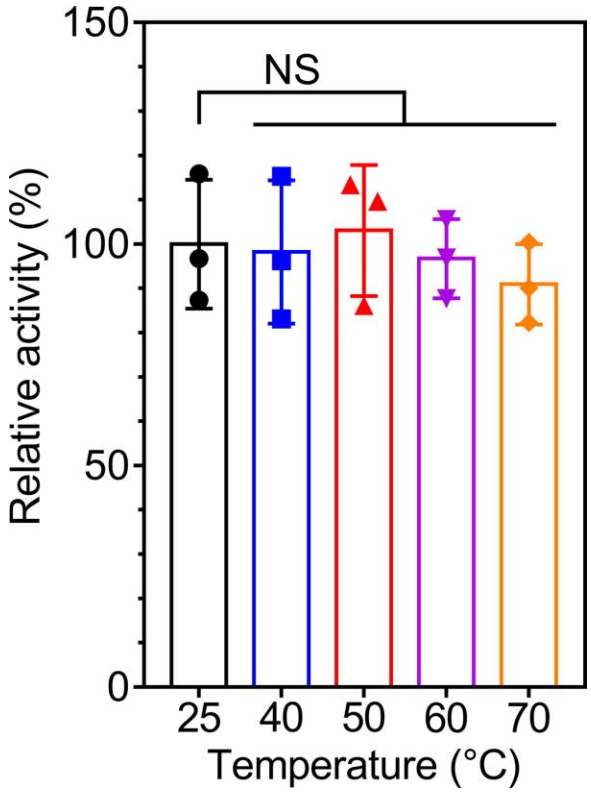

Figure S10. Relative activity of Lyso solutions (100 ppm) after incubation for 2 h at range of temperatures (25, 40, 50, 60, 70 °C) (n = 3). Error bars indicate means ± standard deviations. NS, not significant ($P > 0.05$).

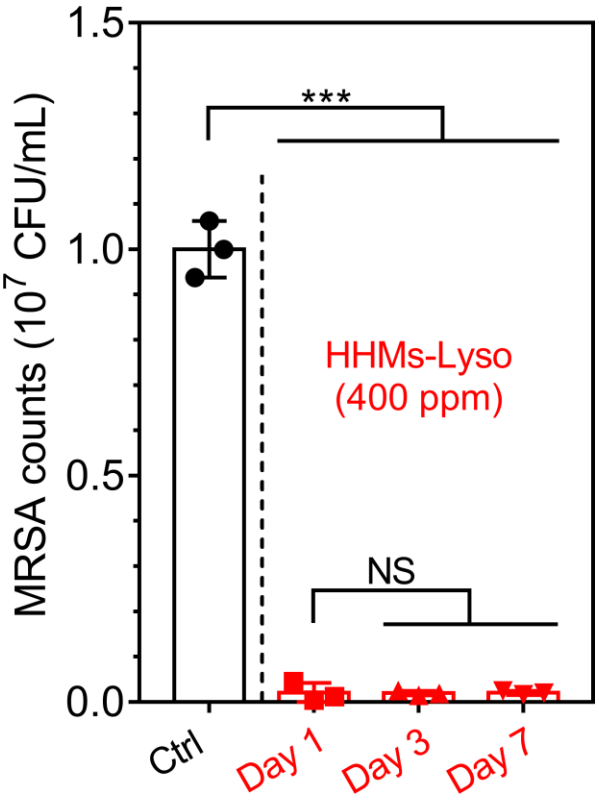

Figure S11. Antibacterial activity of HHMs-Lyso (400 ppm) in L+D2 group (n = 3). Error bars indicate means ± standard deviations: ****P* < 0.001 (t test). NS, not significant (*P* > 0.05).

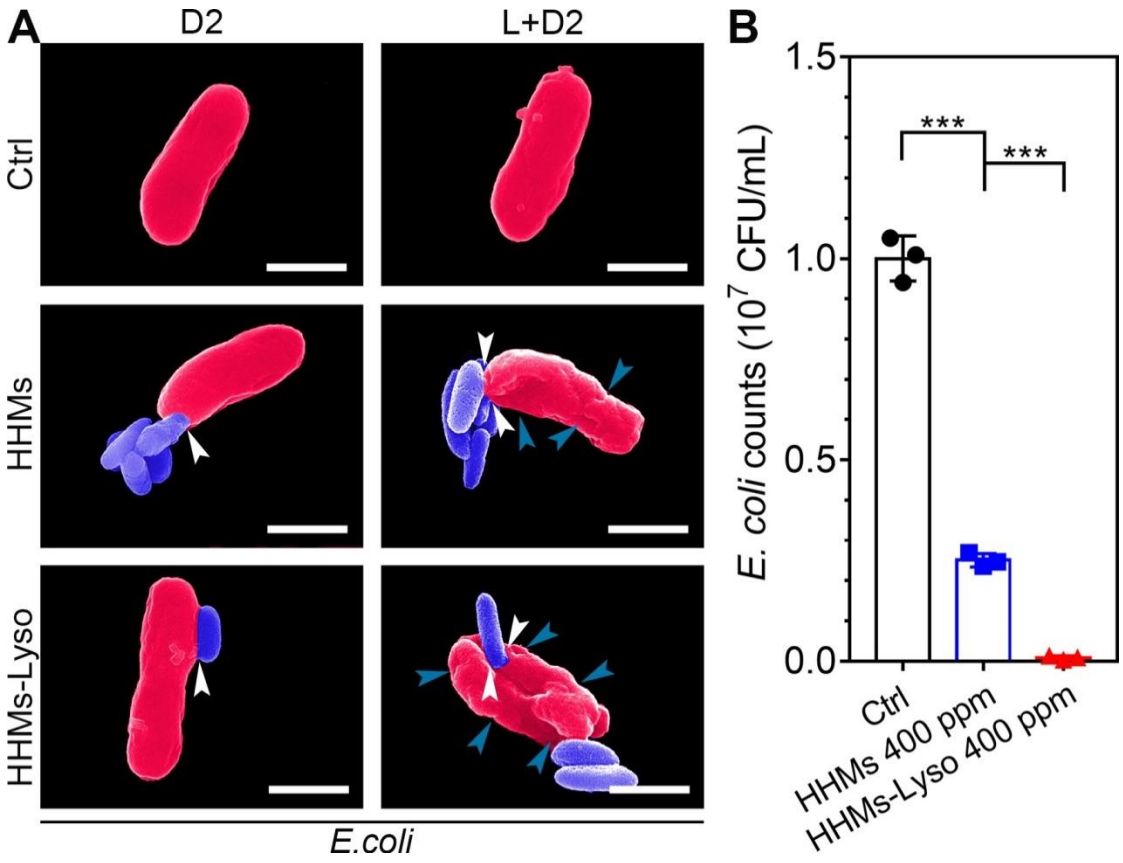

Figure S12. (A) SEM images of *E. coli* morphologies interacted with HHMs and HHMs-Lyso in D2 and L+D2 groups (scale bars = 1 μm). (B) Antibacterial activity of HHMs and HHMs-Lyso in L+D2 group (n = 3). Error bars indicate means ± standard deviations: ***$P < 0.001$ (t test).

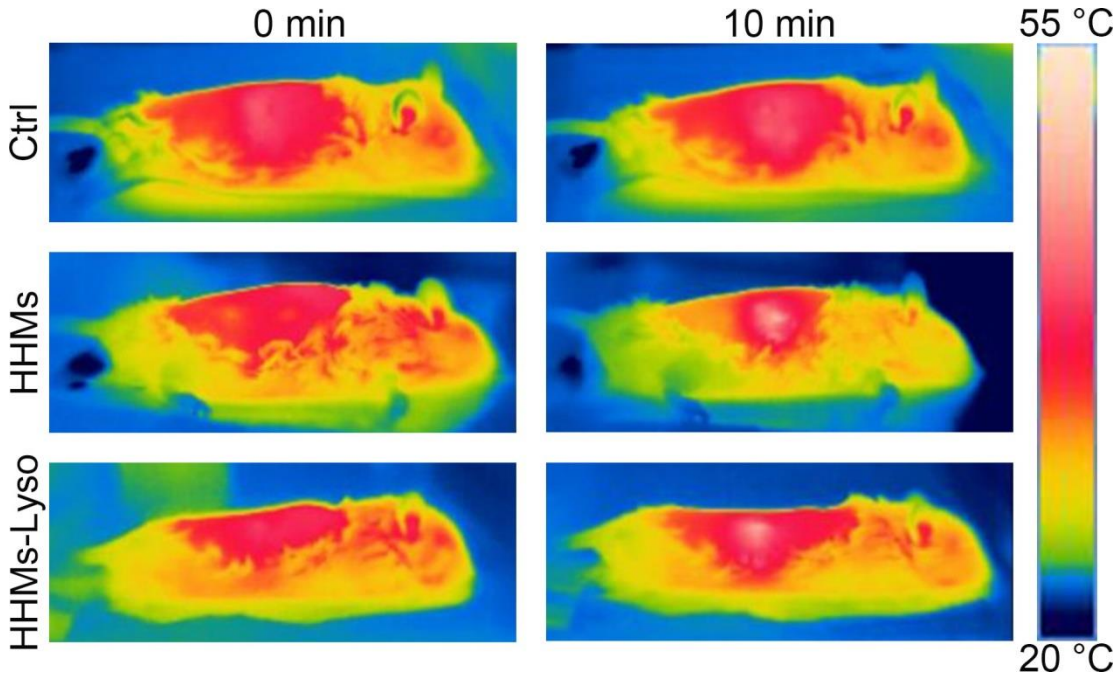

Figure S13. Photothermal images of control, HHMs and HHMs-Lyso during NIR irradiation for 10 min.

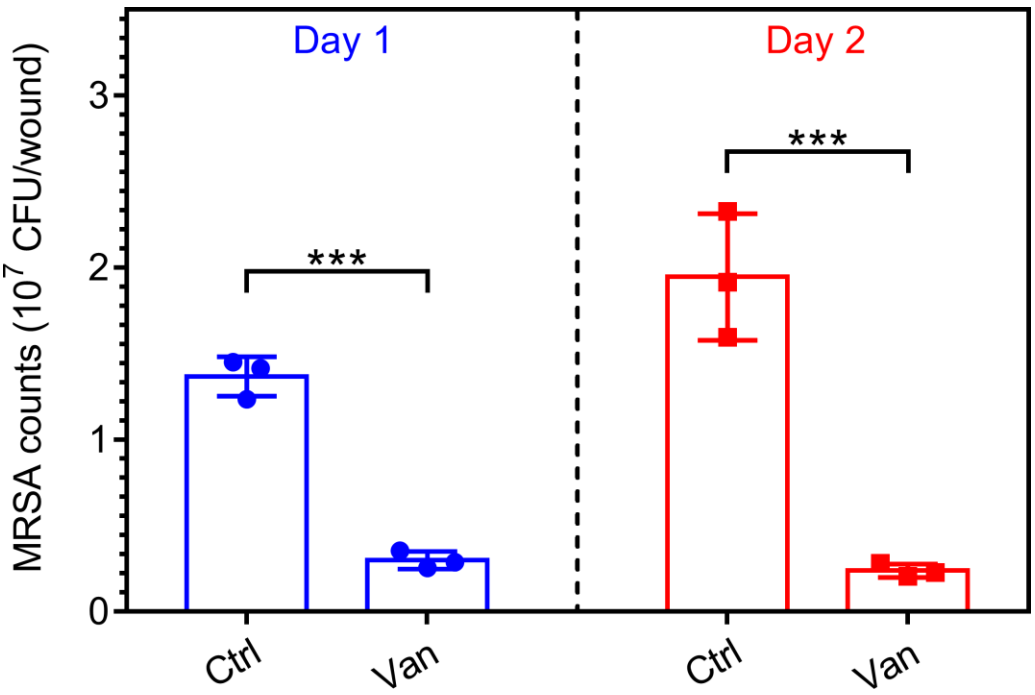

Figure S14. Antibacterial activity by treatment of vancomycin against MRSA infection on day 1 and day 2 (n = 3). Error bars indicate means ± standard deviations: ***$P < 0.001$ (t test).

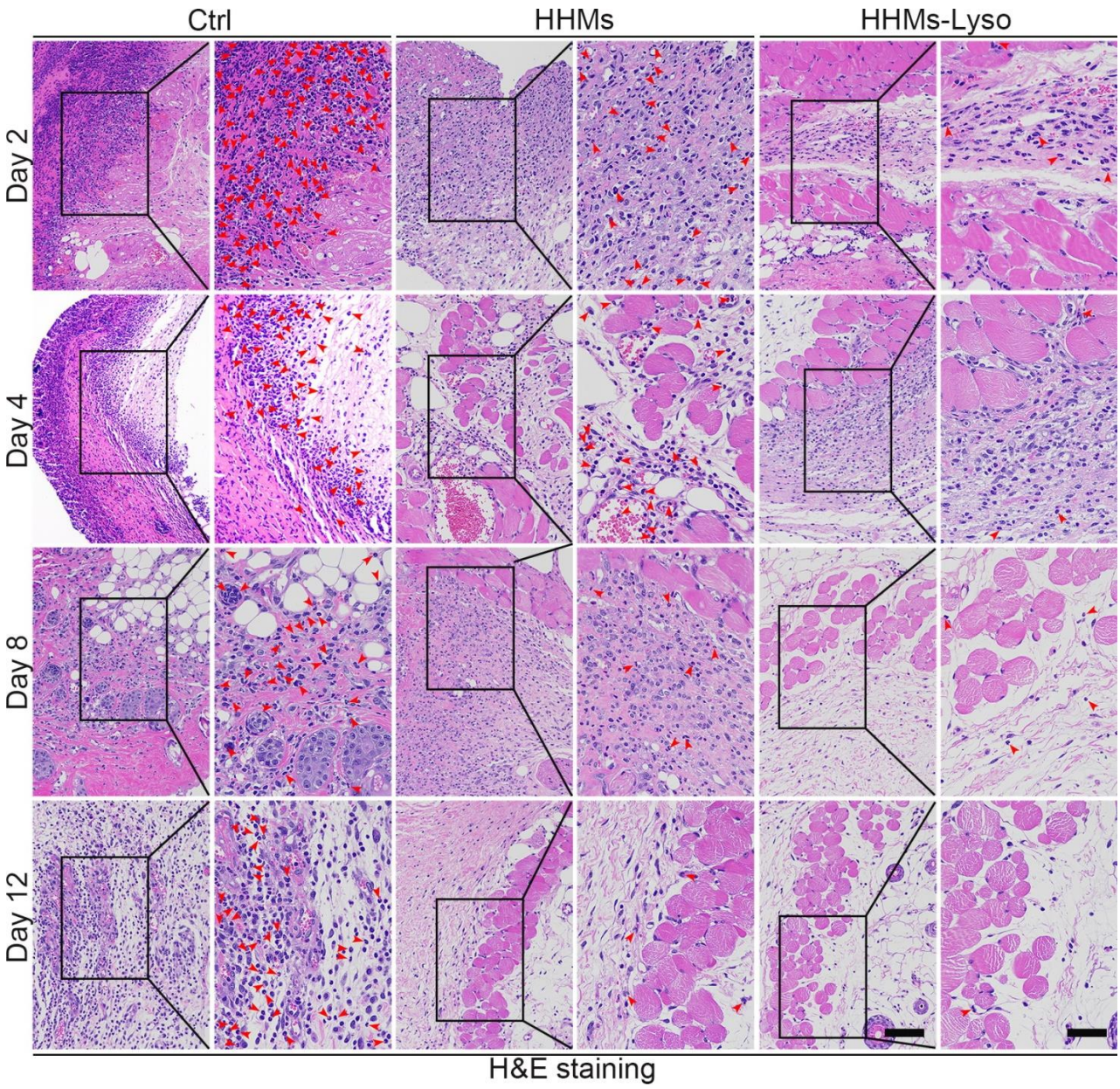

Figure S15. H&E staining (lobulated neutrophils marked by red arrows) of MRSA-infected wounds corresponding to Figure 3I at 2, 4, 8, and 12 days at lower and higher magnification (scale bars = 100 μm and 50 μm, respectively).

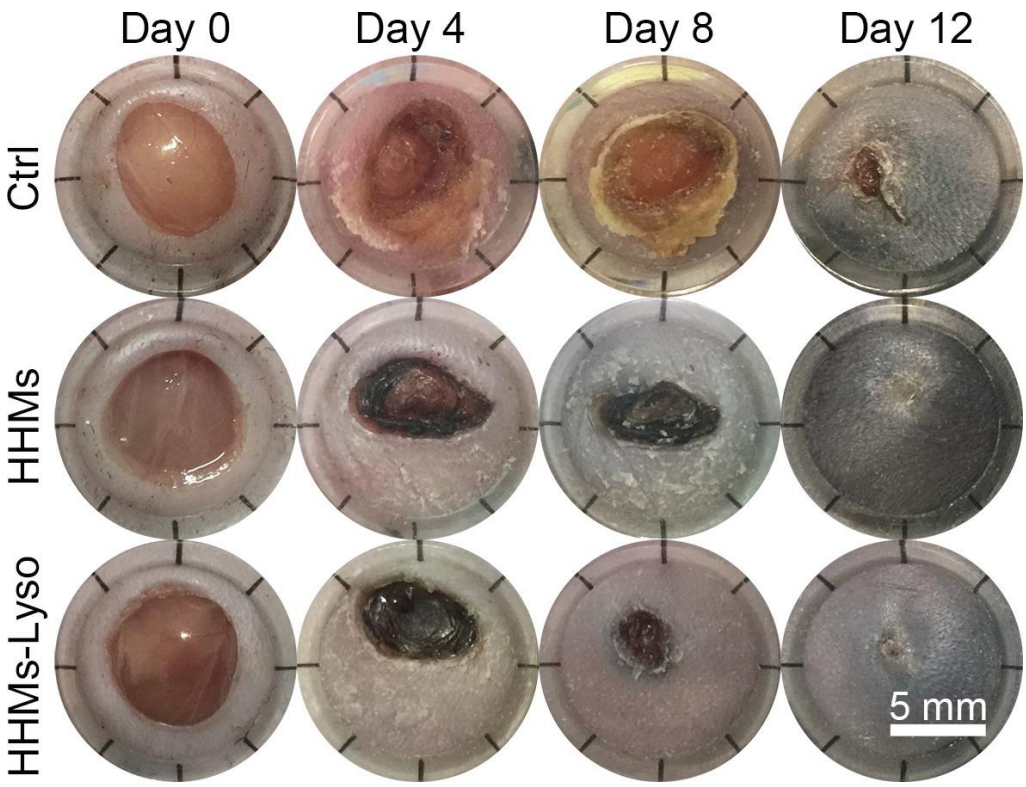

Figure S16. Representative photographs of the wound healing process corresponding to Figure 3J.

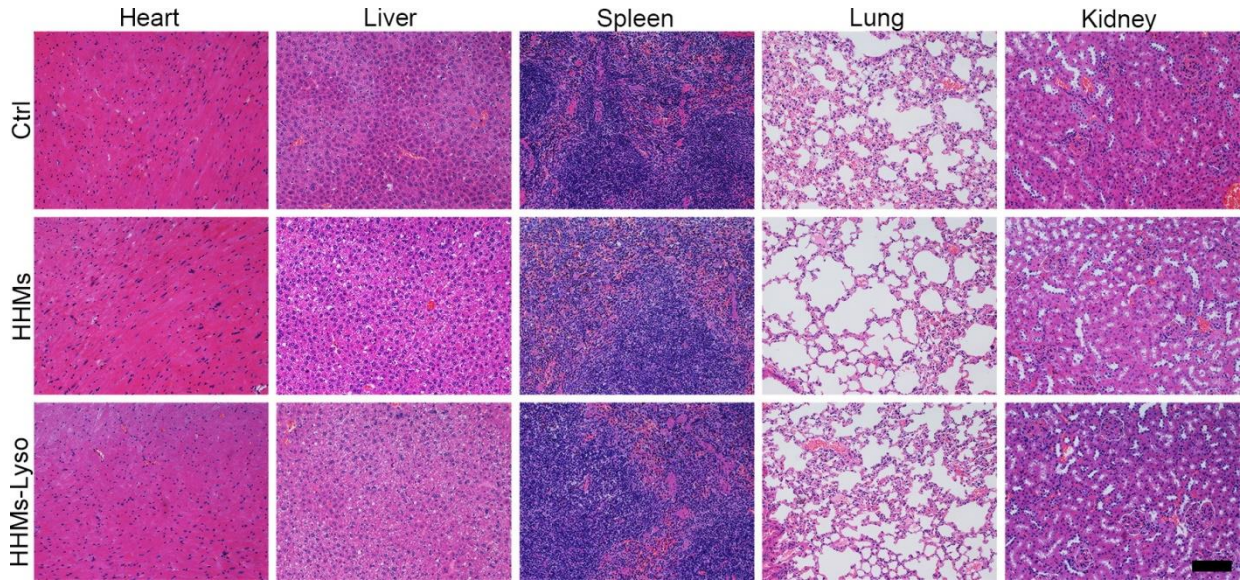

Figure S17. H&E staining of major organs (heart, liver, spleen, lung, and kidney) for *in vivo* toxicology evaluation on day 12 (scale bars = 100 μm).

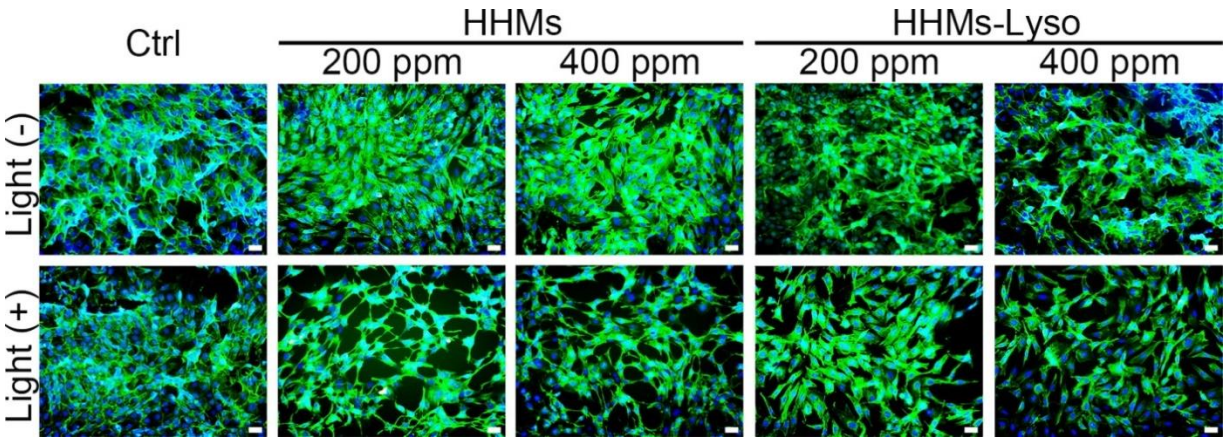

Figure S18. Fluorescent images of NIH3T3 cells after co-cultured with HHMs and HHMs-Lyso (200 and 400 ppm) without or with 808 nm NIR light irradiation to keep 50 °C for 10 min, and follow by incubation for 24 h at 37 °C; F-actin stained with FITC (green) and nucleus stained with DAPI (blue) (scale bars = 50 μm).

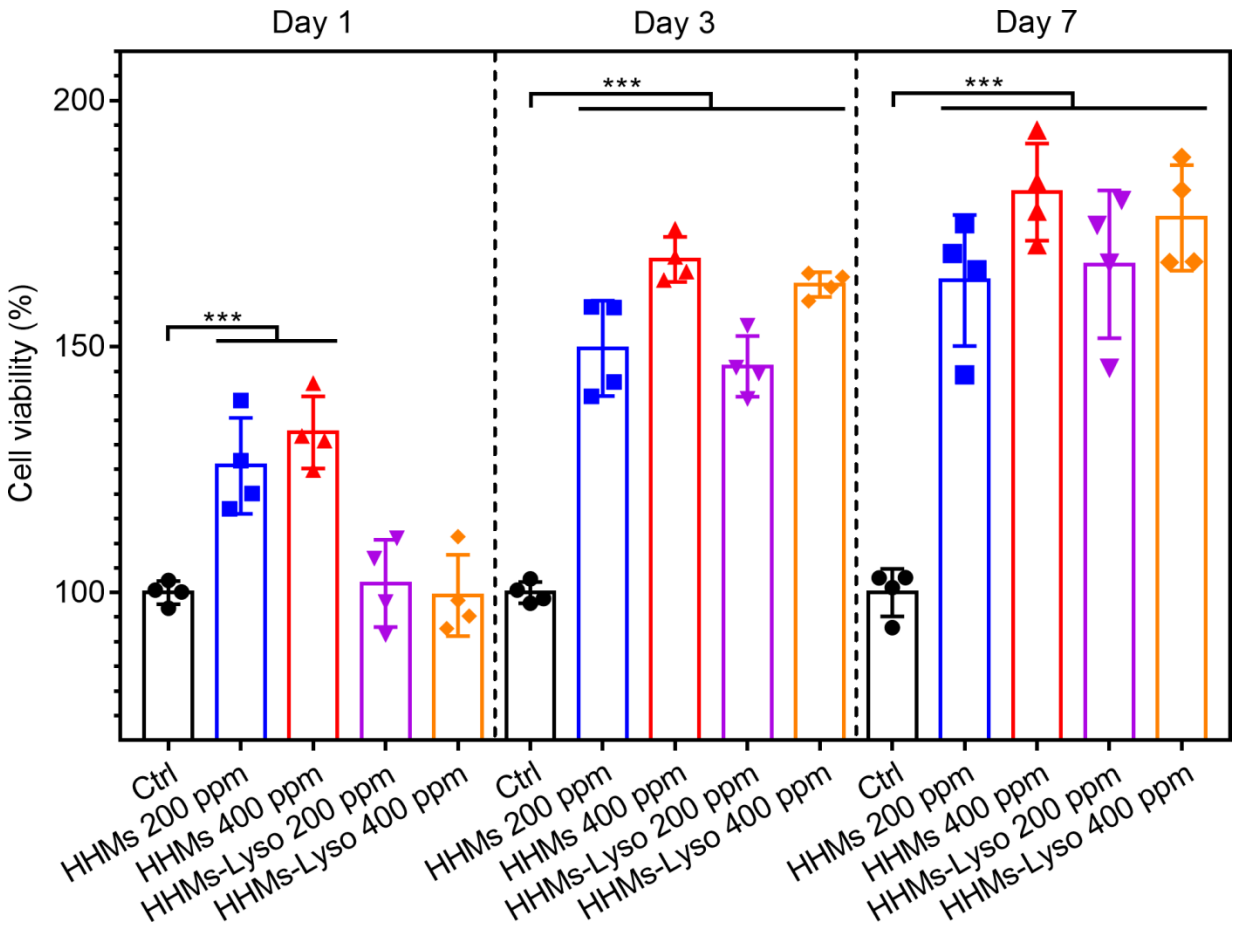

Figure S19. Cell viability of NIH3T3 cells cultured with HHMs and HHMs-Lyso (200 and 400 ppm) for 1, 3, and 7 days (n = 4). Error bars indicate means ± standard deviations: ***$P < 0.001$ (t test).

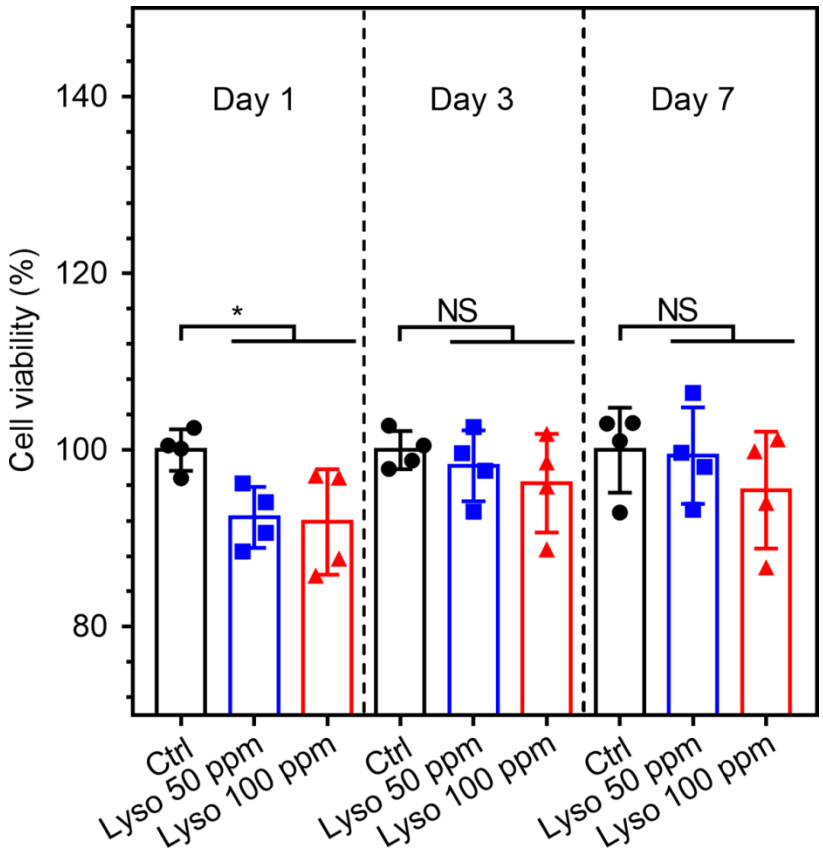

Figure S20. Cell viability of NIH3T3 cells cultured with Lyso (50 and 100 ppm, corresponding to the concentrations in HHMs-Lyso) for 1, 3, and 7 days (n = 4). Error bars indicate means ± standard deviations: **P* < 0.05 (t test). NS, not significant (*P* > 0.05).

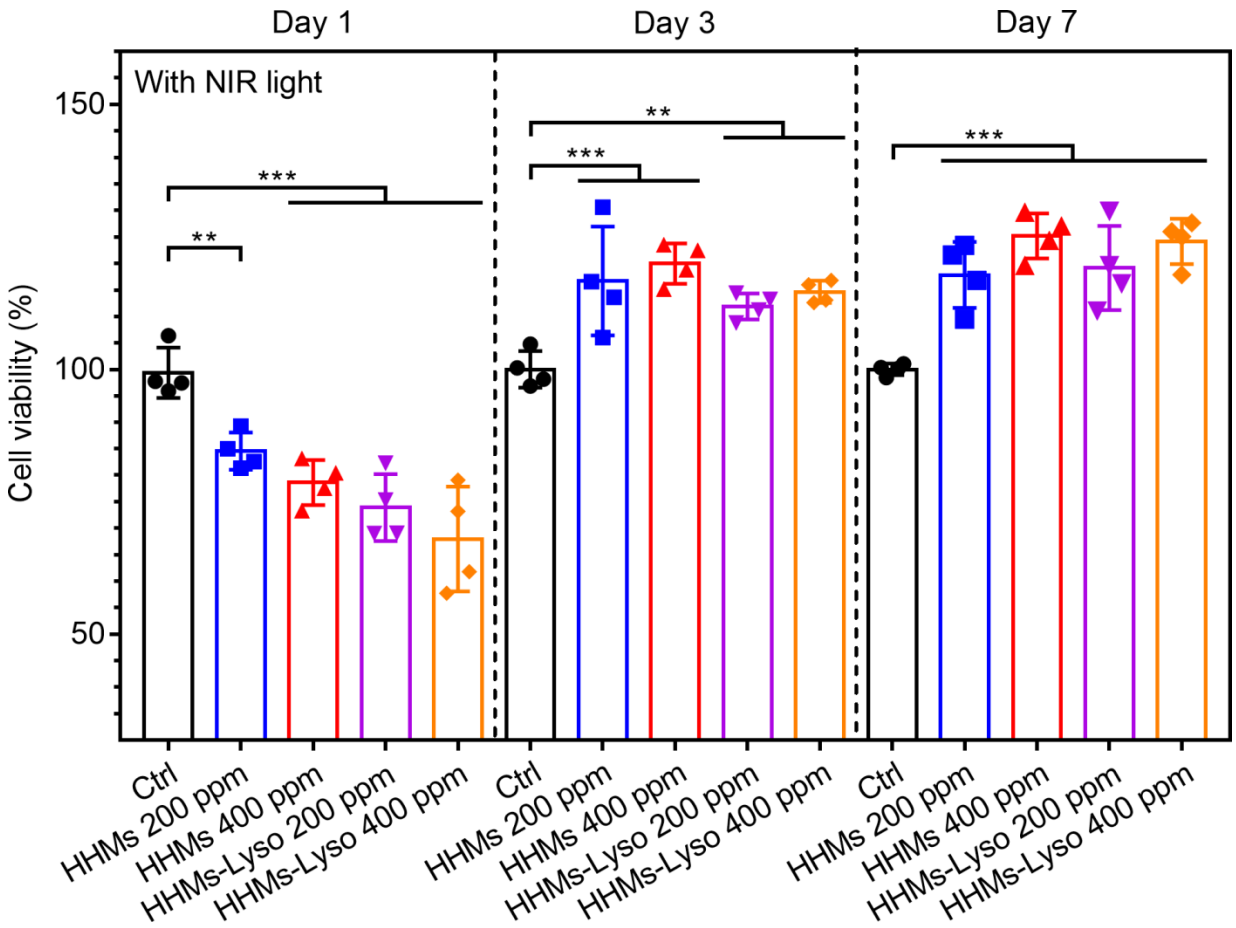

Figure S21. Cell viability of NIH3T3 cells cultured with HHMs and HHMs-Lyso (200 and 400 ppm) after 808 nm NIR light irradiation to keep 50 °C for 10 min, and follow by incubation for 1, 3, and 7 days (n = 4). Error bars indicate means ± standard deviations: $^{**}P < 0.01$, $^{***}P < 0.001$ (t test).

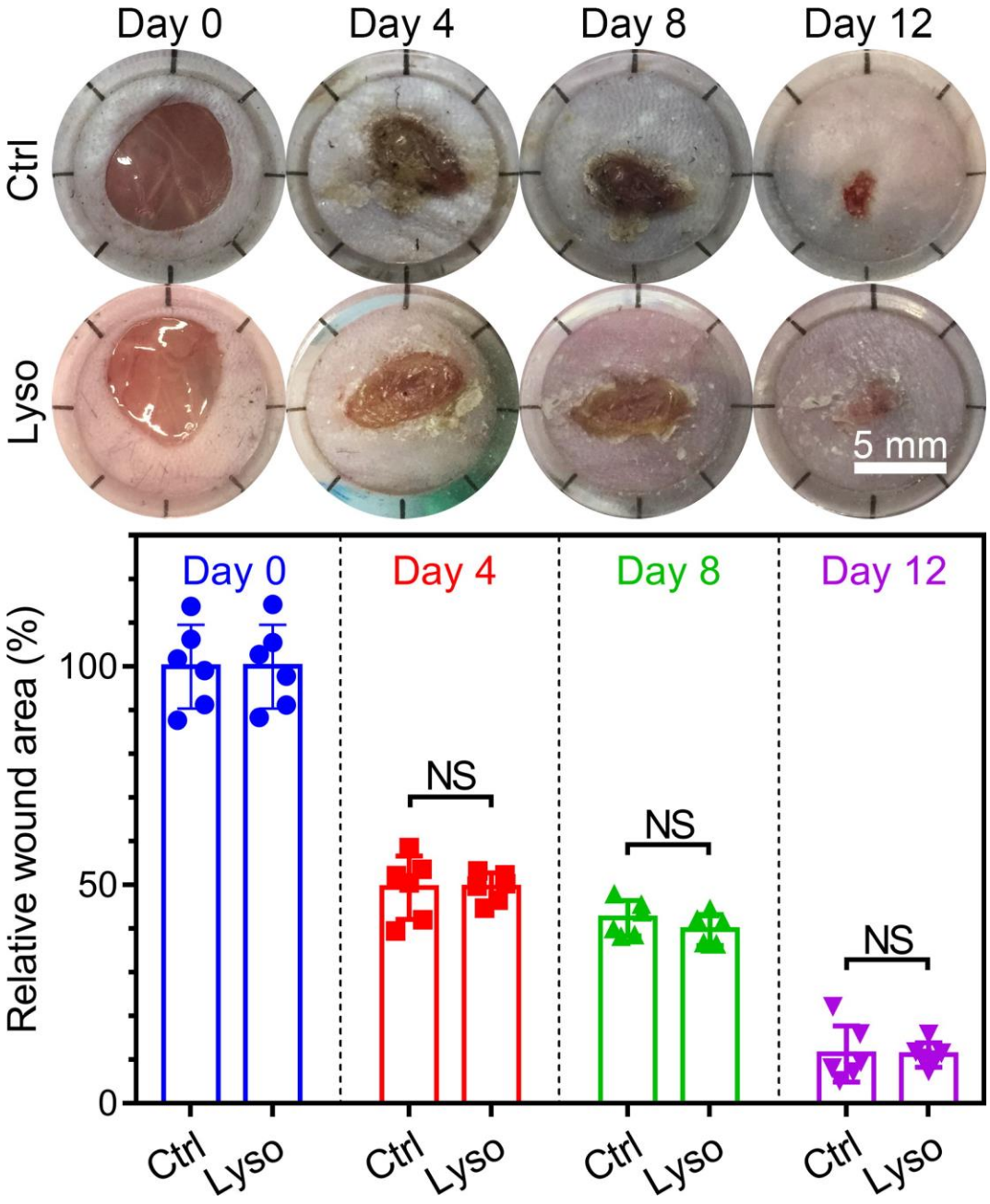

Figure S22. Representative photographs of the wound healing process and quantitative analysis of corresponding images (n = 6). Error bars indicate means ± standard deviations. NS, not significant ($P > 0.05$).

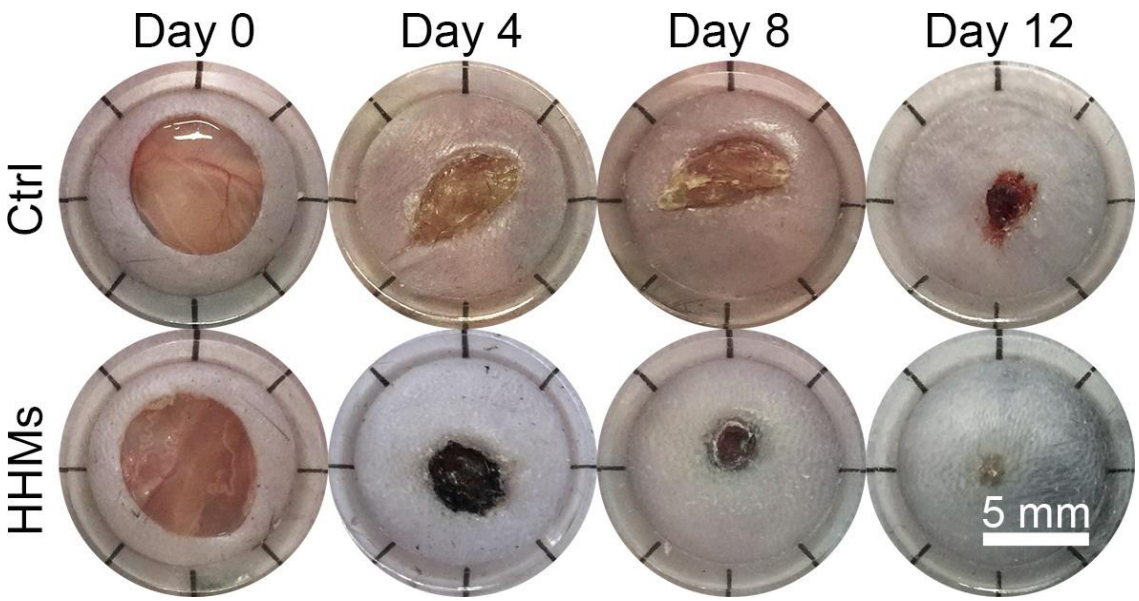

Figure S23. Representative photographs of the wound healing process corresponding to Figure 4A.

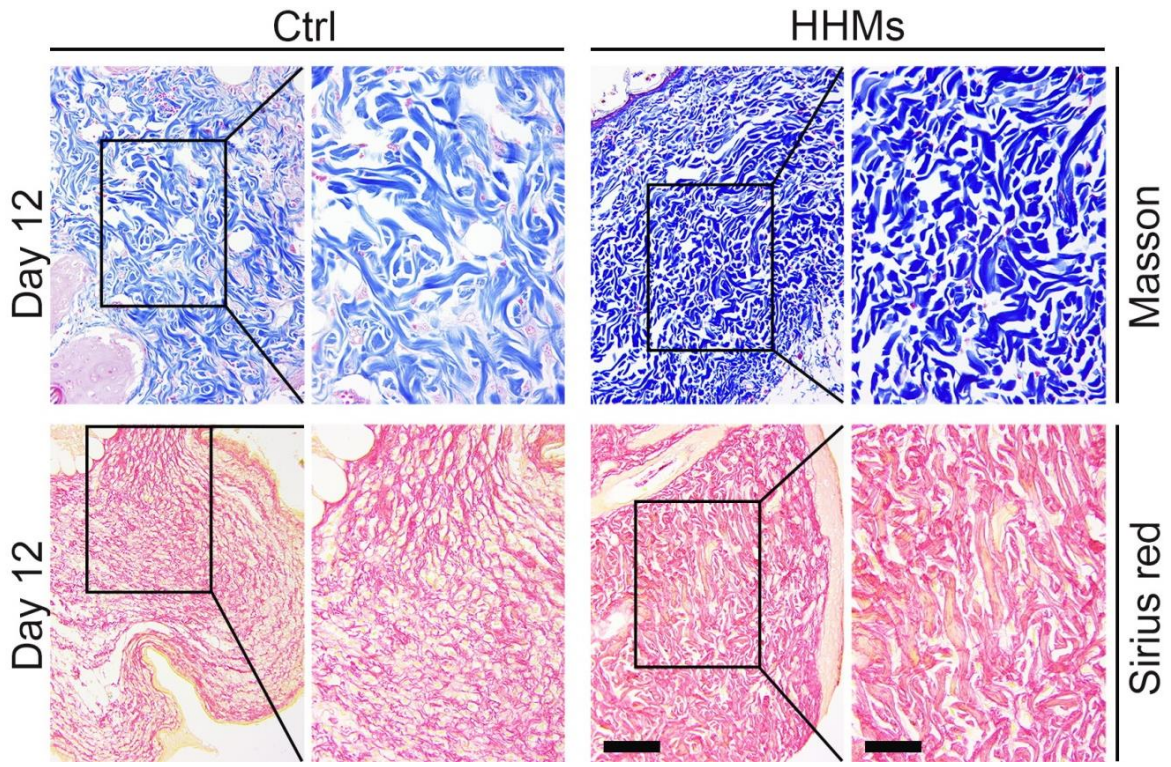

Figure S24. Detection of collagen deposition by Masson's trichrome staining and Sirius red staining corresponding to Figure 4B and Figure 4C on day 12 at lower and higher magnification (scale bars = 100 μm and 50 μm, respectively).

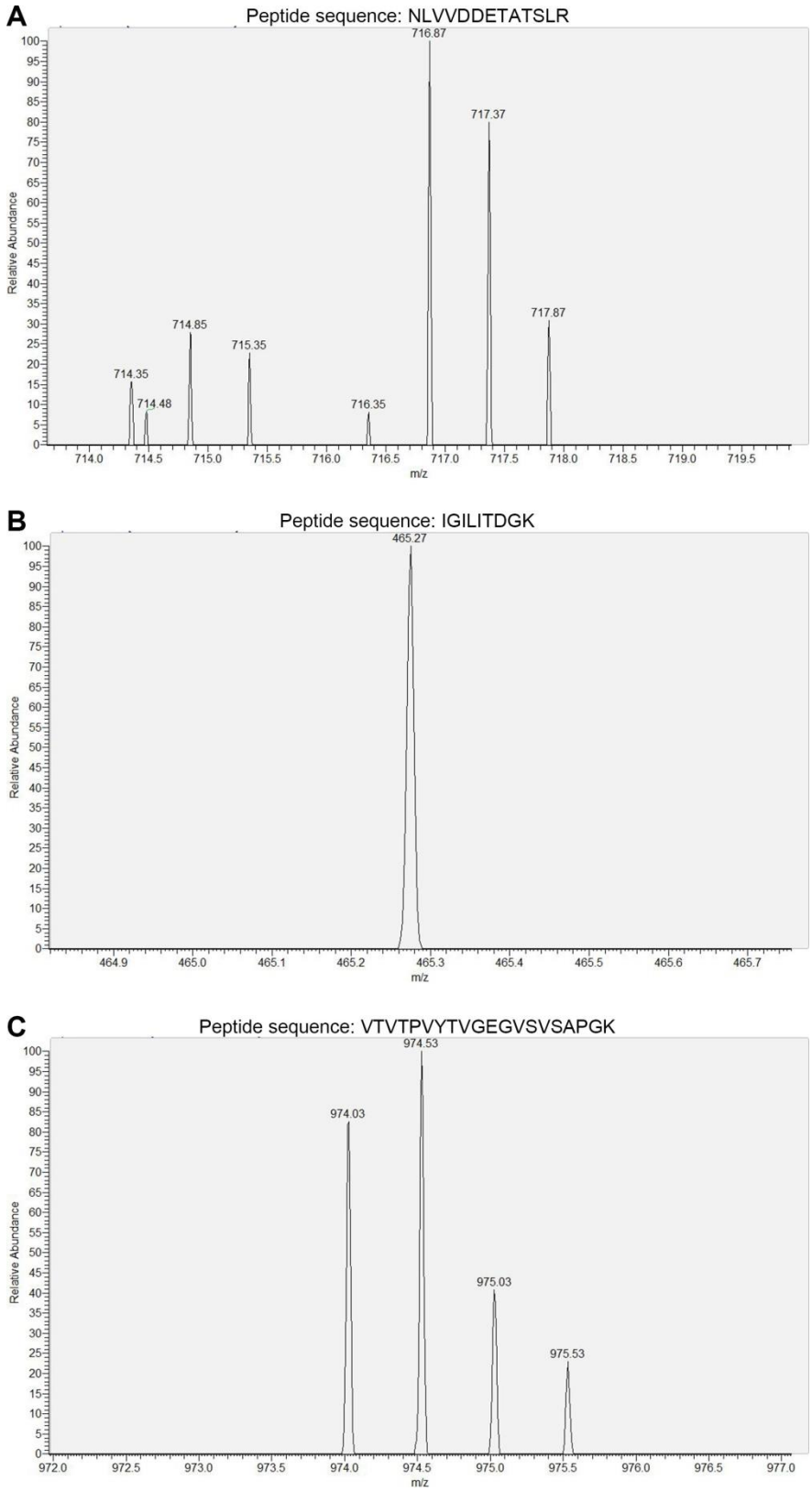

Figure S25. MS spectra of specific peptide sequences (NLVVDDETATSLR, IGILITDGK, and VTVTPVYTVGEGVSVSAPGK) in Col14a1 protein in PRM data analysis.

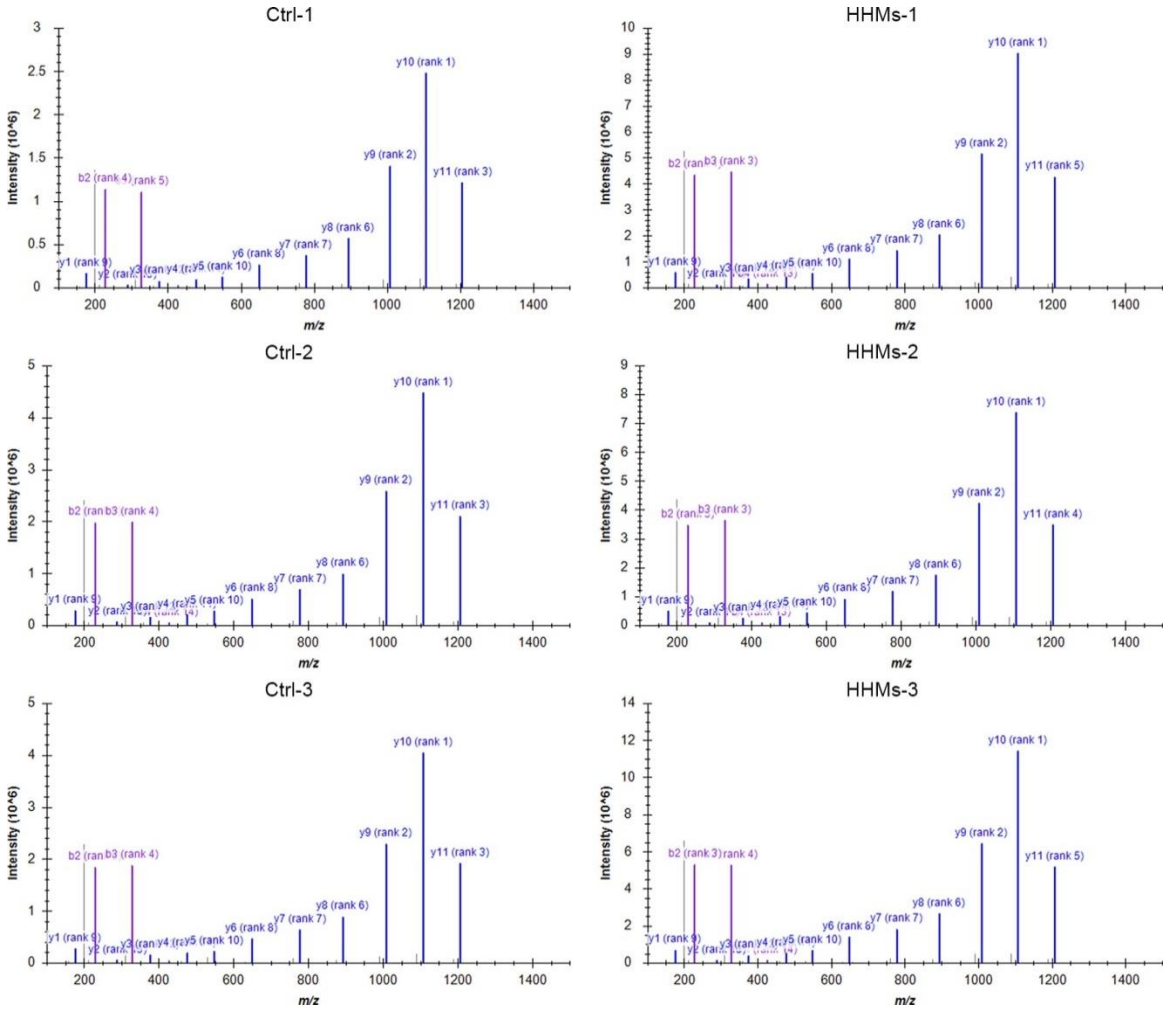

Figure S26. MS/MS spectra of peptide sequence (NLVVDDETATSLR) in Col14a1 protein in PRM data analysis.

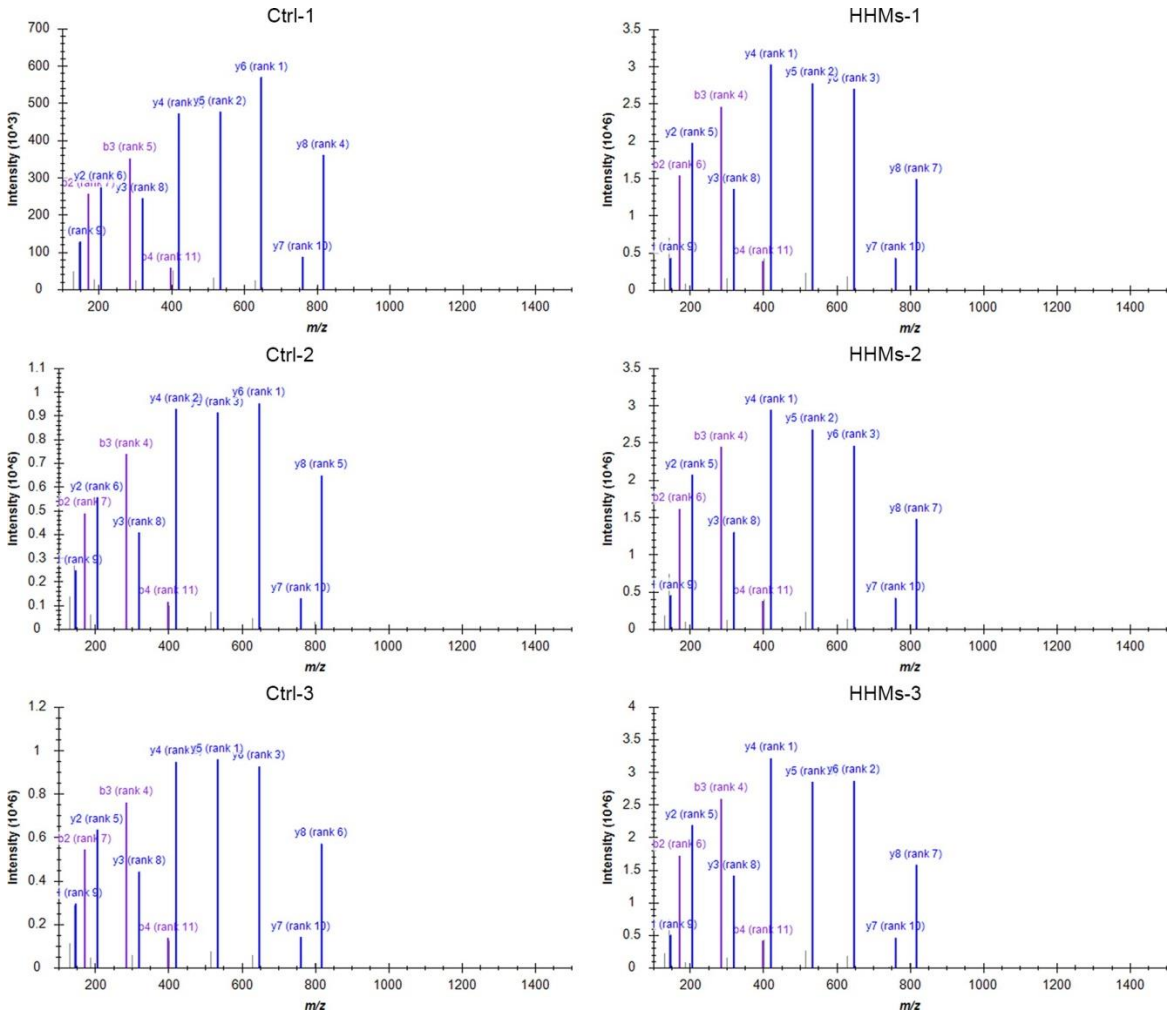

Figure S27. MS/MS spectra of peptide sequence (IGILITDGK) in Col14a1 protein in PRM data analysis.

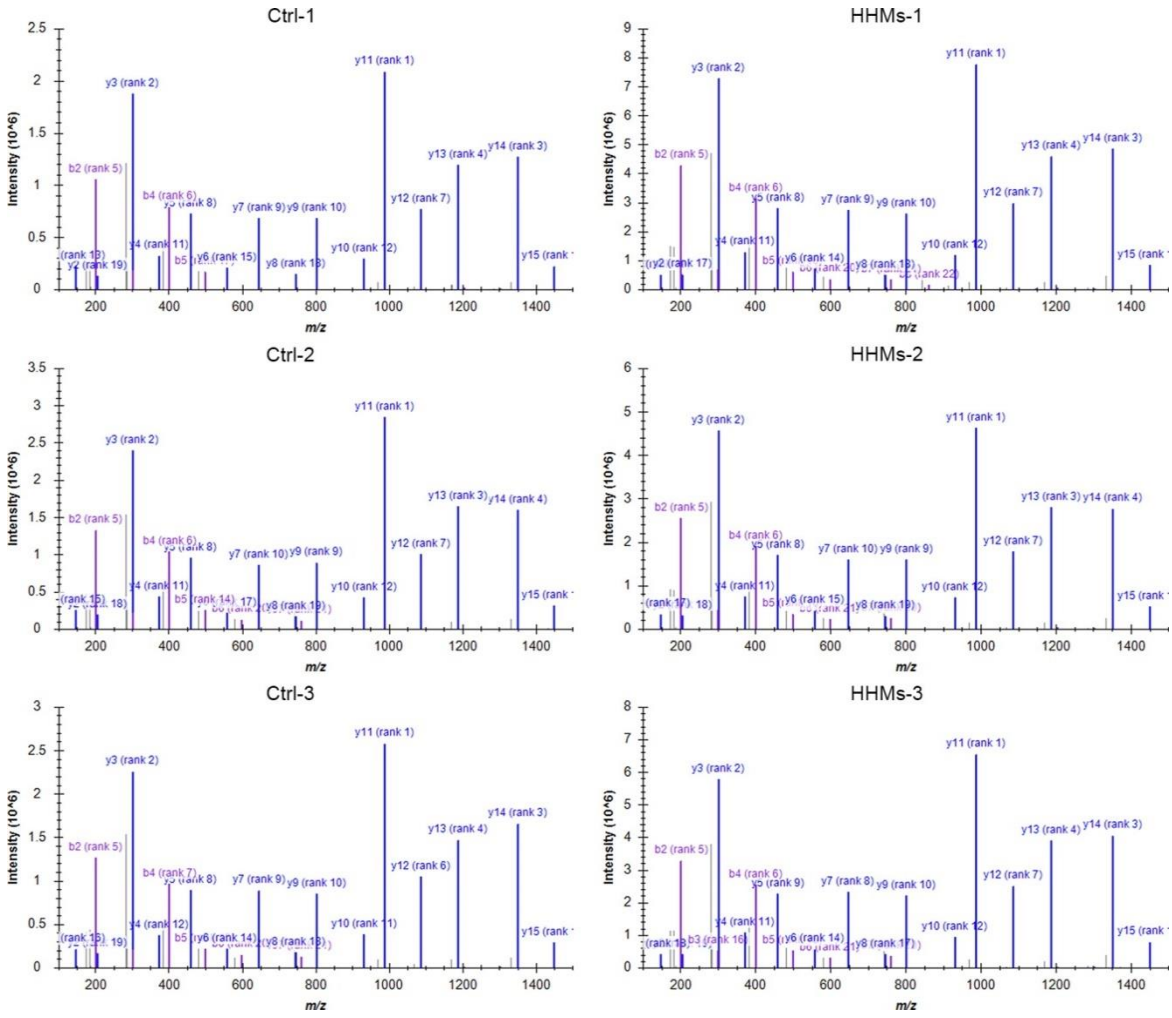

Figure S28. MS/MS spectra of peptide sequence (VTVTPVYTVGEGVSVSAPGK) in Col14a1 protein in PRM data analysis.

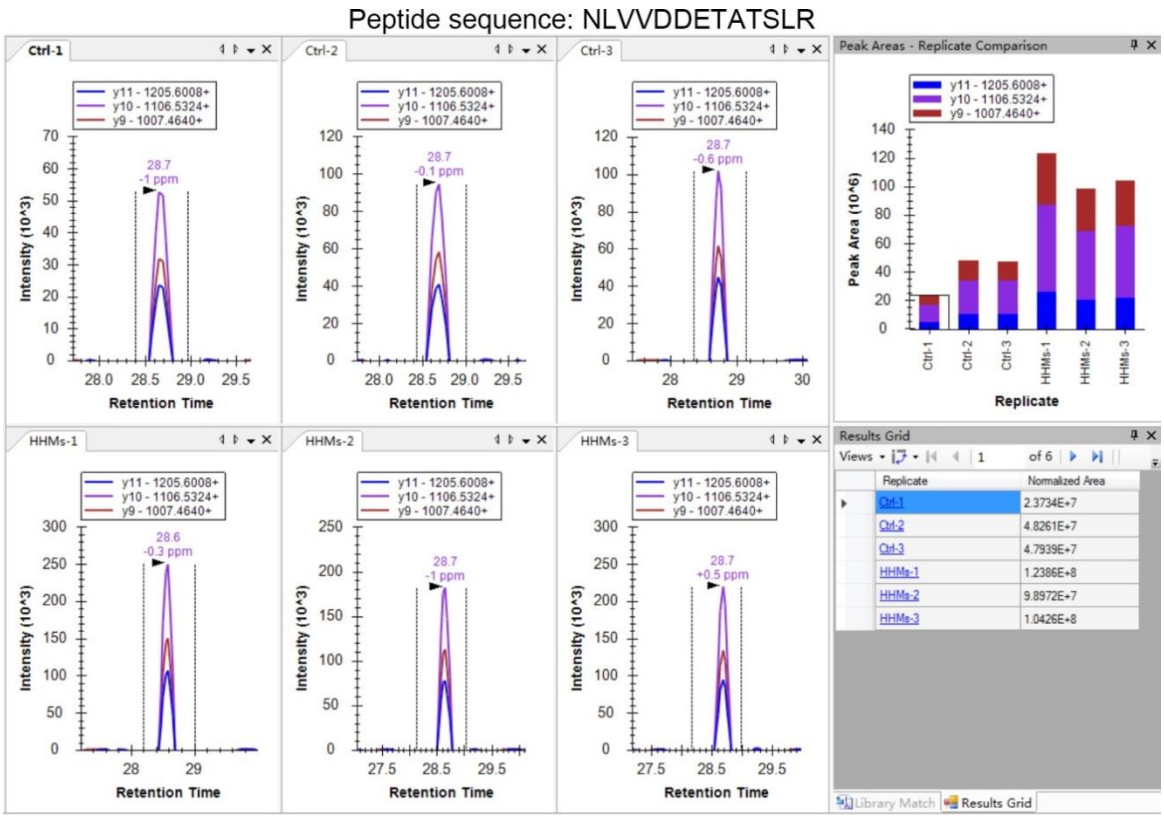

Figure S29. Comparison of peak area of peptide sequence (NLVVDDETATSLR) in Col14a1 protein by PRM data analysis and data integration. All data were analyzed by the Skyline software.

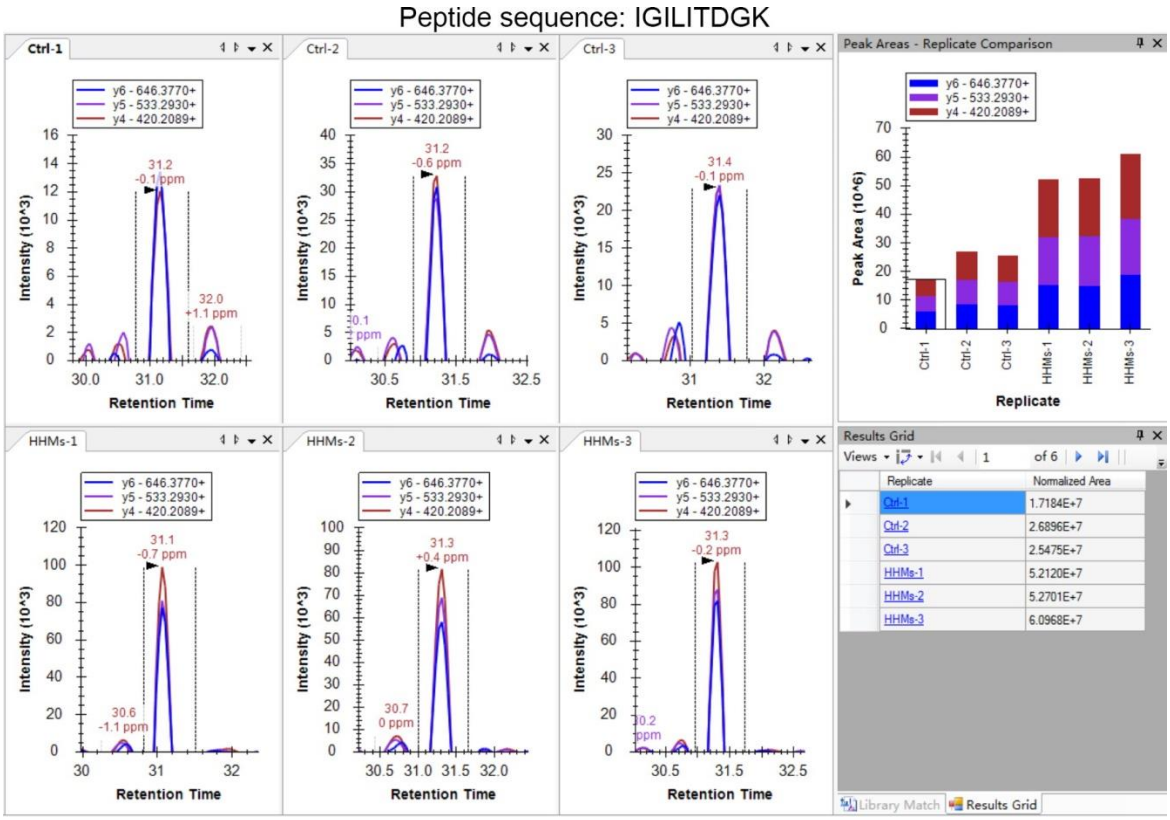

Figure S30. Comparison of peak area of peptide sequence (IGILITDGK) in Col14a1 protein by PRM data analysis and data integration. All data were analyzed by the Skyline software.

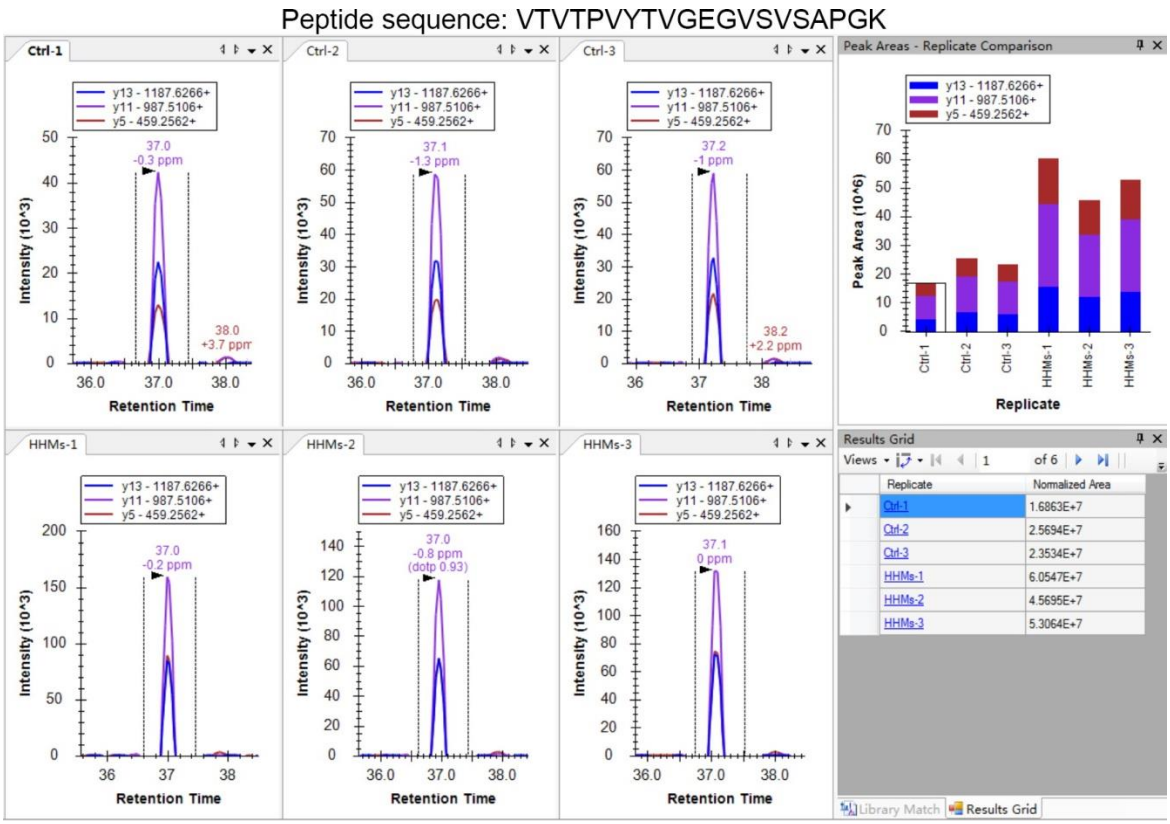

Figure S31. Comparison of peak area of peptide sequence (VTVTPVYTVGEGVSVSAPGK) in Col14a1 protein by PRM data analysis and data integration. All data were analyzed by the Skyline software.

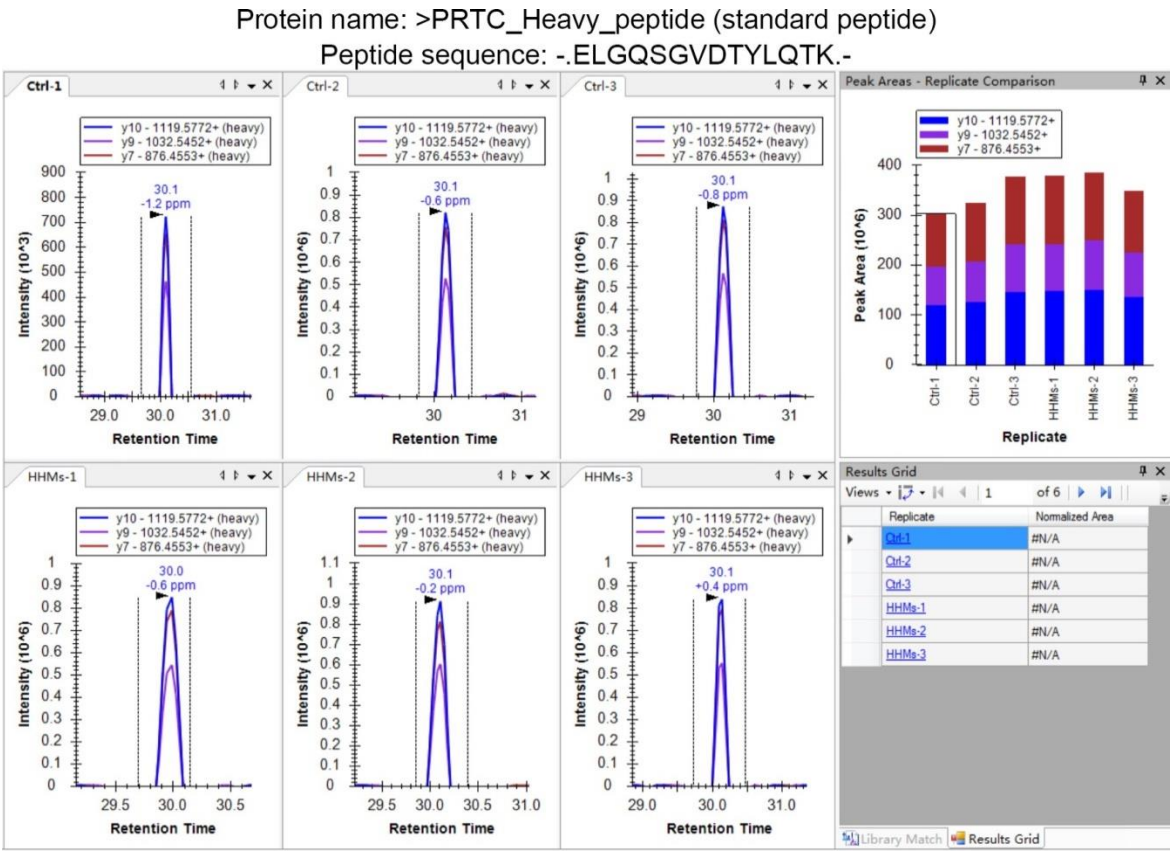

Figure S32. Comparison of peak area of standard peptide sequence (-.ELGQSGVDTYLQTK.-) in Col14a1 protein by PRM data analysis and data integration. All data were analyzed by the Skyline software.

2. Supplementary discussion about Figure 1, Figure S4, **Figure S5**, and **Figure S6**.

The types and contents of amino acids within keratin of HHMs were systematically tested by using an amino acid analyzer machine in **Figure 1E**, where the contents of 17 amino acids have a range from 2% to 18%. Specifically, the contents of the 17 amino acids in order from large to small were as follows: glutamic acid (Glu, 16.58 ± 1.04%), cystine (Cys, 9.33 ± 0.20%), aspartic acid (Asp, 7.47 ± 0.10%), serine (Ser, 6.88 ± 0.15%), leucine (Leu, 6.19 ± 0.35%), glycine (Gly, 5.96 ± 0.05%), arginine (Arg, 5.77 ± 0.11%), phenylalanine (Phe, 5.71 ± 0.16%), proline (Pro, 5.46 ± 0.16%), valine (Val, 4.40 ± 0.15%), tyrosine (Tyr, 4.34 ± 0.13%), alanine (Ala, 4.34 ± 0.03%), isoleucine (Ile, 3.46 ± 0.27%), methionine (Met, 3.42 ± 0.03%), lysine (Lys, 2.55 ± 0.14%), threonine (Thr, 2.46 ± 0.01%), and histidine (His, 2.09 ± 0.05%).

Figure S4 shows that HHMs in PBS in a horizontal shaker at 37 °C suffer relatively rapid degradation compared with those in water without shaking at room temperature over 8 weeks. Specifically, the changes in color, morphology, and absorbance were negligible on day 7 in **Figure S4**A and **Figure S4**B, suggesting that HHMs maintain the relative stability during the initial 1 week in DI water. Over time, the absorbance of the HHMs gradually deteriorated for 8 weeks, accompanied by color fading and obvious morphological changes due to the gradual degradability of HHMs. In **Figure S4**C, the hydrodynamic sizes of HHMs measured by DLS gradually decreased over time, indicating the slow degradation of HHMs. By contrast, as shown in **Figure S4**D and **Figure S4**E, the relatively rapid biodegradability of the HHMs in PBS over 8 weeks was confirmed by the faster color fading, more obvious

morphological changes, and lower absorbance than those in DI water. Particularly, the HHMs were almost fully degraded after 8 weeks in PBS because the color of 200 ppm HHMs was nearly transparent with the minimum absorbance and the morphology of the HHMs was mostly disrupted. The relative percentages of degradation of HHMs are generally calculated according to the absorbance at 808 nm in the curves in **Figure S4**B and **Figure S4**E, where the relative percentage of degradation of HHMs in PBS (56.23%) is higher than that in DI (32.18%) on Day 56. Besides, in **Figure S4**F, the degradability of the HHMs into smaller nanoparticles in PBS was more rapid than that in DI water in **Figure S4**C, where the medium of PBS and the mechanical shake at 37 °C would accelerate the degradability of the HHMs. HHMs can be degraded into the smaller nanoparticles *in vitro* in the absence of proteinase. Consequently, the HHMs have proper biodegradation behavior in a time-dependent manner with the characteristics of short-term relative stability and long-term biodegradation. Similarly, as shown in **Figure S5**, the stability of HHMs-Lyso has the same tendency with that of HHMs. The stability of HHM-Lyso will be further discussed below.

Based on the above analysis of the results, the possible process of biodegradability of the HHMs in a physiological environment is illustrated in **Figure S4**G. The physiological environment is more complex than the above model of biodegradation *in vitro*. When the HHMs are in the physiological environment, the external keratins of HHMs by specific proteolytic enzymes will be gradually degraded into peptide segments and amino acids due to hydrolysis of the peptide bond. Additionally, a

possible pathway for melanin biodegradation *in vivo* is the oxidation-induced degradation process in the presence of oxidizing agents, where many biologically generated active oxygen species in the human body are formed by a family of multisubunit enzymes, such as nicotinamide adenine dinucleotide phosphate (NADPH) oxidases.[24] In order to simulate this pathway, H_2O_2 solutions with different concentrations are selected as an oxidizing agent to evaluate the biodegradability of melanin in HHMs. In **Figure S6**, the intensities of absorption spectra of the HHMs (200 ppm) in H_2O_2 solutions gradually decrease with the increase of the concentration of H_2O_2 solutions (1, 10, 100, 1000 mM) on Day 2, confirming that the melanin in HHMs has oxidation-induced degradation in the presence of oxidizing agents. Therefore, the internal melanin in HHMs will be decomposed into segments (reduced molecular weight), oligomers and monomers, and finally degraded into carbon dioxide and water. Thus, the final degradation products from the HHMs in the physiological environment are biocompatible peptides, amino acids, CO_2, and H_2O, all of which are commonly found in the human body. In summary, natural biodegradable HHMs have great potential in biomedical applications *in vivo* because the proper biodegradability of the HHMs not only avoids rapid degradation but also allows total clearance from the body in a reasonable period after fulfilling their therapeutic functions.